A Numerical Investigation of Collision Efficiencies of Simple Ice Plates Colliding With Supercooled Water Drops

R. L. PITTER[1] AND H. R. PRUPPACHER

Dept. of Meteorology, University of California, Los Angeles 90024

(Manuscript received 2 July 1973, in revised form 16 October 1973)

ABSTRACT

The hydrodynamic interaction between simple ice plates, idealized as oblate spheroids of axis ratio 0.05, and water drops, assumed to be spherical, was numerically investigated for atmospheric conditions of −10C and 700 mb. The ice plates had semi-major axis length between 147 and 404 μm and the water drops had radii up to 53 μm. Since the ratio of the mass of the drop to the mass of the crystal was small, the superposition model was found to be satisfactory. The flow fields around drops were those of LeClair *et al.*, and the flow fields around oblate spheroids were those of Pitter *et al.* From the trajectories of the water drops relative to the ice crystals, collision efficiencies were determined. The model predicts preferential riming of the drops at the edges of crystals under certain conditions, in agreement with field observations in atmospheric clouds.

1. Introduction

The riming process between ice crystals and water drops is of considerable importance in atmospheric clouds because it is the process by which ice crystals grow to graupel particles and hailstones. This has been recognized as a very efficient mechanism in the formation of precipitation-size particles, and several attempts have therefore been made at incorporating it in dynamic models of clouds.

In two earlier studies (Braham, 1968; Takeda, 1968a, b), the growth of spherical ice crystals by collision with water drops was computed using the formulas of Langmuir (1948). Thus, ice crystals were assumed to have collision efficiencies similar to those of water drops of the same size. In a more recent attempt, Musil (1970) looked at the growth of hailstones in feeder clouds, assuming that the ice crystal collision efficiencies with water drops varied linearly from 0.5 to 1.0 for ice embryos between 20 and 45 μm radius, and was unity for larger ice crystals. Another attempt at simulating mixed cloud development was made by Danielson *et al.* (1972). In this model all ice crystals were assumed to be spheres. A stochastic growth equation was used for both water drop collision-coalescence and ice crystal riming. The stochastic growth equation utilized a collection kernel which was assumed to be identical for ice crystals as for water drops of the same size.

Numerous investigations reported in literature [for a summary, see Mason (1971)] have shown that the basic shape of an ice crystal growing by diffusion is that of a hexagonal prism. Depending on temperature, the ice crystals possess either prominent *c*-axis growth (columns) or *a*-axis growth (thin plates). Thus, the assumption of spherical ice particles, made in the investigations mentioned above, is unjustified. Recently, there have been some attempts to obtain collision efficiencies for bodies of ice crystal shape. Ono (1969) and Wilkins and Auer (1970) suggested the use of collision ecffiiencies derived by Ranz and Wong (1952) on the basis of invicid flow past disks. However, since atmospheric ice crystals typically have Reynolds numbers <100, potential theory is not justified. Also, the settling velocity of water drops is neglected by such treatment. For hexagonal columns, Ono derived collision efficiencies based on the results of Davies and Peetz (1956), who applied creeping flow to Reynolds number 0.2 and numerically determined flow at Reynolds number 10 for an infinitely long circular cylinder.

Since glaciation in atmospheric clouds is frequently initiated by aerosol particles at temperatures between −10 and −18C, atmospheric ice crystals predominantly have *a*-axis growth, and assume shapes of thin hexagonal plates with or without dendritic extensions. This motivated us to study the collision behavior of plate-like ice crystals with water drops as a first step in a study of the riming behavior of ice crystals. Jayaweera and Cottis (1969) and List and Schemenauer (1971) have experimentally shown that the hydrodynamic behavior of a simple hexagonal plate can be approximated with sufficient accuracy by that of a circular disk. Pitter *et al.* (1973) showed that the

[1] Present affiliation: Department of Environmental Technology, Oregon Graduate Center for Study and Research, Beaverton 97005.

hydrodynamic behavior of an oblate spheroid is the same as that of a circular disk of the same aspect ratio. For these reasons, we computed the collision efficiencies of water spheres with ice oblate spheroids of axis ratio 0.05 and have assumed that these collision efficiencies closely approximate those for thin hexagonal plates of ice.

2. The superposition model

Klett and Davis (1973) have discussed in detail the difficulties associated with the exact determination of collision efficiencies for two interacting spheres falling under the influence of gravity in an otherwise undisturbed fluid. They have also discussed the simplifications which can be made in order to solve the collision efficiency problem and the cost of such simplications to the physical realism of the problem.

In order to model the hydrodynamic interaction of two spheres with as much physical realism as possible, they used an analytical method, based on a modified form of the Oseen equations for the flow field, and simultaneously satisfied the changing boundary conditions at the surfaces of the two spheres during the interaction. While such an analytical treatment would also be highly desirable for the case of hydrodynamic interaction between an ice crystal and a water drop, the complex geometry associated with this interaction presently prohibits it.

We therefore chose the so-called superposition scheme, which models such interactions though it neglects the close boundary effects, since it assumes that each body moves in the stream caused by the fluid motion around the other body in isolation (Shafrir and Neiburger, 1963; Shafrir and Gal-Chen, 1971). This approach does not give accurate accounts of the hydrodynamic interaction when the two bodies are very close to each other, especially when they fall with similar velocities. Indeed, comparison of the results derived from the superposition scheme for colliding spheres with the analytical results of Klett and Davis and the experimental results of Woods and Mason (1965) show that the objections to this method are valid when the bodies have similar fall velocities.

However, we feel there are reasons for believing that the superposition model is reasonably accurate in the case of interactions between a thin ice crystal and a water drop. It can be shown that the total energy associated with the flow field around a falling drop or ice crystal is proportional to the square of the vorticity of the flow field, and hence proportional to the drag force on the body considered. Since accelerations which occur during a hydrodynamic interaction of the falling bodies are small as compared to mg, where m and g are the mass of the body and the acceleration of gravity, the total energy associated with the flow field is approximately proportional to the mass of the body (Steinberger *et al.*, 1968; Klett, 1968). Consequently, a reasonable parameter for evaluating the effect of the smaller body's flow field on the larger body is the mass ratio of the two bodies. Field observations by Wilkins and Auer (1970) and Ono (1969) show that simple ice plates begin riming at a radius between 100 and 150 μm. Thus, the present study of the collision efficiency was conducted for oblate spheroids of axis ratio 0.05 and semi-major axis length between 147 and 404 μm. Water spheres investigated ranged between 6 and 53 μm radius for the largest oblate spheroid. Considering those sizes of spheres which collided with oblate spheroids, the mass ratio of the interacting bodies, $m_S/m_L=a_S^3\rho_{\text{water}}/(a_L^3AR\rho_{\text{ice}})$, never exceeded 0.05. Consequently, for the interactions investigated, the effect of the sphere's flow field on the oblate spheroid was vanishingly small, even though the velocity ratio of the interacting water drop and ice crystal was as high as 0.8. Thus, it is felt that the use of the superposition model to obtain collision efficiencies for oblate spheroids of ice interacting with water spheres is justified. This is supported by the fact that collision efficiencies computed by Shafrir and Neiburger, and Shafrir and Gal-Chen for interacting spheres using the superposition model exhibited fair agreement with the analytical methods of Klett and Davis and the experimental results of Beard and Pruppacher (1971), Woods and Mason (1964) and Picknet (1960) for intermediate and small values of p [$=a_S/a_L$, where a_S and a_L are the radii of the small and large spheres, respectively], when a_L was greater than 30 μm.

The above argument also provides justification for neglecting the possibility of the flow field around the drop causing the crystal to tilt. Since angular acceleration is proportional to the torque and inversely proportional to the moment of inertia of the body, while the moment of inertia of the oblate spheroid of ice is proportional to the mass of the oblate spheroid, and since the torque on the spheroid is due to the effect of the flow field around the sphere and consequently is proportional to the energy in the wake of the sphere, it becomes apparent that the ability of the water sphere to cause angular accelerations of the ice spheroid is approximately proportional to the mass ratio of the bodies. Since the mass ratio was always small in the present investigations, tilting of the oblate spheroid was unlikely to occur.

3. Results and discussion

Eq. (16) [see Appendix] was numerically integrated to obtain critical grazing trajectories. From the initial critical offsets, the collision efficiency was determined by Eq. (20). In order to compute the collision efficiencies, it was necessary to determine the size and terminal velocity of each oblate spheroid of ice, given the axis ratio, Reynolds number, and drag coefficient of the oblate spheroid, and atmospheric conditions of −10C and 700 mb. Size and terminal velocity were

computed from Eqs. (13) and (14). It was necessary to determine whether terminal velocities computed in this manner applied also to thin hexagonal plates with aspect ratios of 0.05. For this purpose, the terminal velocities for the oblate spheroids of ice were also computed for atmospheric conditions of −10C and 1000 mb for comparison. Excellent agreement was found between the terminal velocities calculated from the present results and the experimental values for simple hexagonal plates of aspect ratio 0.04–0.05 as measured experimentally by Jayaweera and Cottis (1969), and to simple hexagonal plates of ice as measured by Kajikawa (1972) for atmospheric conditions of −10C.

Fig. 1 displays collision efficiencies of ice oblate spheroids interacting with water spheres, plotted against drop radius a_S. Fig. 2 displays the same collision efficiencies plotted against the velocity ratio $V_{S\infty}/V_{L\infty}$. The most noticeable features in Figs. 1 and 2 are the cutoffs at large and small drop sizes. Applying the results of Figs. 1 and 2 to the atmosphere, it is apparent that each collecting thin ice plate has a drop size range outside of which it has zero collision efficiency. It is noticed that as the crystal size increases, the largest size of water drop which can collide with the crystal also increases. Investigation of the effect of the small-drop cutoff on the evolution of mixed clouds reveals some interesting results. In a cloud containing a narrow drop size spectrum of very small drop sizes, the ice crystals must grow by diffusion to relatively large sizes in order for riming to commence. This is illustrated by the result that an oblate spheroid of ice with a 160-μm semi-major axis can collect water spheres down to 12.9 μm radius, while oblate spheroids of ice of 194, 213, 289 and 404 μm can collect drops down to 9.6, 8.6, 7.2 and 6.3 μm radius, respectively. In addition to the cutoffs at large and small drop size, Fig. 1 shows there

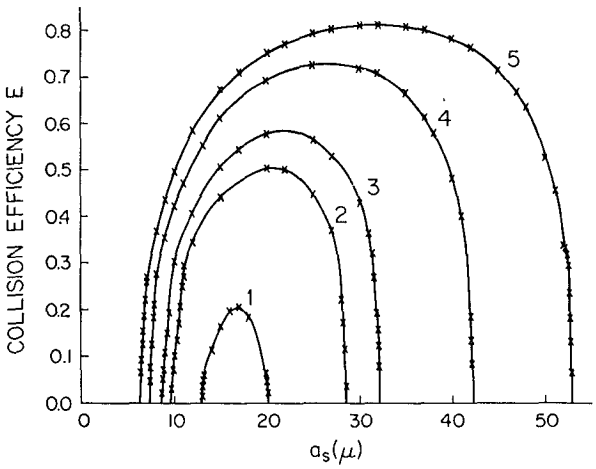

FIG. 1. Variation of the collision efficiency of an oblate spheroid of ice with water sphere radiüs: (1) $a_L=160$, (2) $a_L=194$, (3) $a_L=213$, (4) $a_L=289$, (5) $a_L=404$ μm.

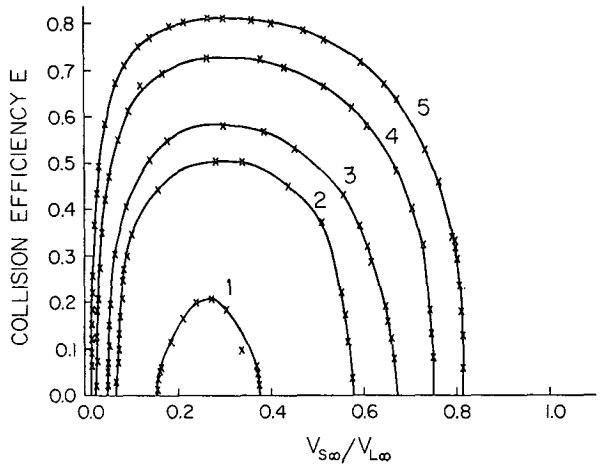

FIG. 2. Variation of the collision efficiency of an oblate spheroid of ice with terminal velocity ratio of sphere to oblate spheroid: (1)$a_L=160$, (2) $a_L=194$, (3) $a_L=213$, (4) $a_L=289$, (5) $a_L=404$ μm.

is a minimum spheroid size below which an oblate spheroid of ice will not be able to collect any size water sphere. The present results place this minimum size between 147 and 160 μm for the semi-major axis. This range agrees excellently with the field observations of Wilkins and Auer (1970) and Ono (1969) who both found that simple hexagonal plates of ice had to be larger than 150 μm radius in order to be able to collide with supercooled water drops. Consequently, independent of the drop-size distribution in clouds, simple hexagonal plates of ice must grow such that the semi-major is 150 μm long before they can begin to grow by riming. Fig. 1 also reveals that the efficiency of colliding with a given size water sphere increases as size of the oblate spheroid of ice increases. The maximum values of collision efficiencies are greater for larger oblate spheroids of ice, and they occur at larger sizes of water spheres. As an example, for a 160-μm oblate spheroid, the maximum occurs at a 17 μm radius sphere and has the value of 0.205, while for a 404-μm oblate spheroid, the maximum occurs at a 32 μm radius sphere and has a value of 0.808. It is seen from Fig. 2 that for any size oblate spheroid, maximum collision efficiency occurs near a terminal velocity ratio of 0.29.

4. Investigation of cutoffs

The cutoffs in collision efficiency occurring at large and small water sphere sizes (Figs. 1 and 2) required more detailed investigation. It was found that y_c, previously defined as the initial offset of the critical grazing trajectory, outside of which collision never occurred and inside of which collision always occurred, was an insufficient parameter for determining collision efficiencies. Water spheres of certain sizes were found which would not collide inside of some inner critical offset, denoted $y_{\min}$. Since $y_{\min}<y_c$, the region of initial

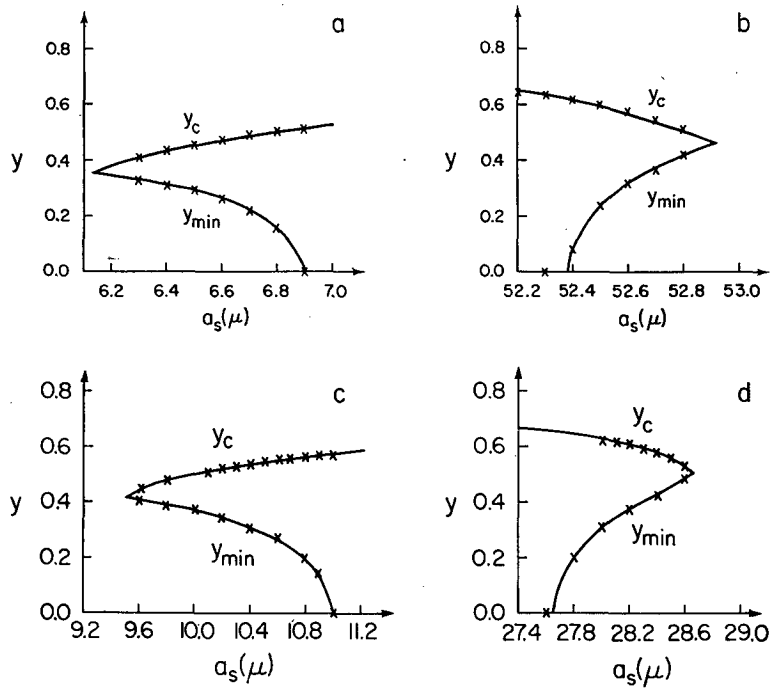

FIG. 3. Variation of y_c and y_{min} with radius of water sphere: (a) $a_L=404$ μm, small water spheres; (b) $a_L=404$ μm, large water spheres; (c) $a_L=194$ μm, small water spheres, (d) $a_L=194$ μm, large water spheres.

offsets resulting in collision, termed the collision domain of the oblate spheroid of ice, is the area $\pi y_c^2-\pi y_{min}^2$ in a horizontal plane sufficiently far removed upstream from the oblate spheroid [see Eq. (20) in the Appendix]. Thus, if $y_{min}=0$, the collision domain beneath the oblate spheroid of ice can be pictured in three dimensions as a circular cylinder with its axis on the axis of symmetry of the oblate spheroid, and with its upper end flared outward and terminated at the oblate spheroid. When $y_{min}>0$, the collision domain can be pictured as a circular annulus of radii y_{min} and y_c, again with its upper end flared outward and terminated at the oblate spheroid. Annular collision domains were found only for sphere sizes near the cutoffs of the collision efficiency curves, except for an oblate spheroid of 160 μm semi-major axis, where the annular behavior occurred at all sizes of collected drops. At the small sphere cutoff, variations of y_c and y_{min} with a_S are given in Figs. 3a and 3c for ice spheroids with semi-major axes of 404 and 194 μm, respectively. At the large

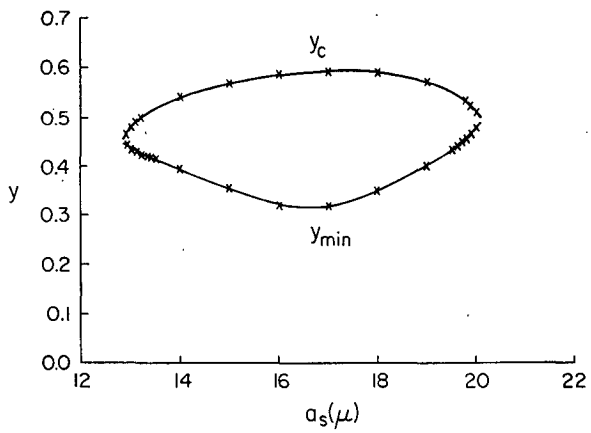

FIG. 4. Variation of y_c and y_{min} with water sphere radius for $a_L=160$ μm.

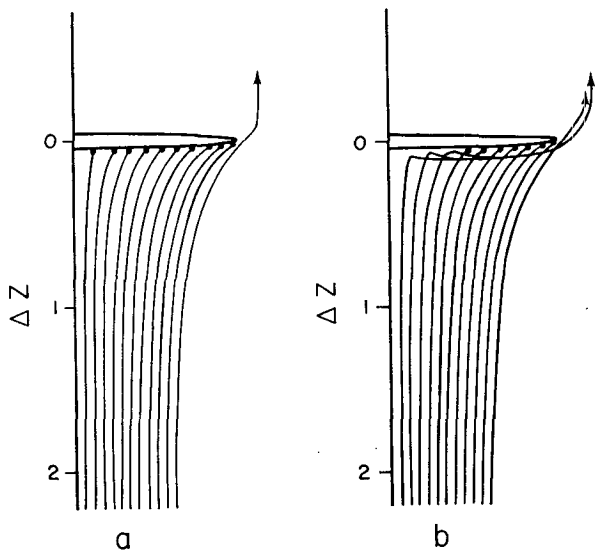

FIG. 5. Trajectories of water spheres relative to a 404-μm oblate spheroid of ice: (a) $a_S=7$, (b) $a_S=6.8$ μm.

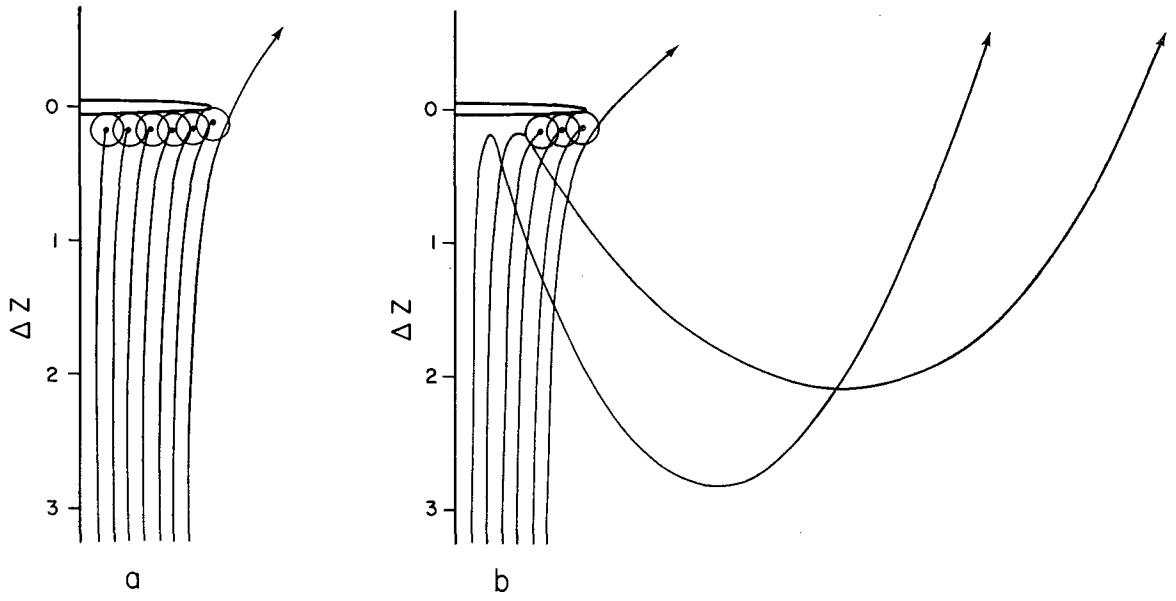

FIG. 6. Trajectories of water spheres relative to a 404-μm oblate spheroid of ice: (a) $a_S=52$, (b) $a_S=52.5$ μm.

sphere cutoff, variations of y_c and $y_{\min}$ with a_S are given in Figs. 3b and 3d for the same sizes of oblate spheroids. It is seen from this figure that the span of sphere sizes associated with the annular domains increases from 0.6 to 1.4 μm at the small sphere cutoff and from 0.5 to 1.0 μm at the large sphere cutoff as the size of the oblate spheroid decreases from 404 to 194 μm. As the oblate spheroid size decreases to near the minimum collecting size, the annular behavior spreads to the entire range of colliding sphere sizes. Fig. 4 depicts y_c and $y_{\min}$ for a 160-μm oblate spheroid of ice. In order to visualize the structure of the annular collision domain in another manner, it is useful to examine several sets of trajectories of the water spheres relative to the oblate spheroid of ice. For example, such sets were constructed for spheres of 7 and 6.8 μm radius interacting with a 404-μm oblate spheroid of ice (Fig. 5). Similarly, trajectories were constructed for water spheres of 52 and 52.5 μm radius interacting with a 404-μm oblate spheroid of ice (Fig. 6). The annular behavior of the 6.8 and 52.5 μm radius spheres is clearly demonstrated. The water spheres do not collide at $y<y_{\min}$ or $y>y_c$.

A detailed study was undertaken to verify the physical reasons for the annular behavior which occurs at some sizes of spheres and oblate spheroids. Although the actual study was quite involved, the basic procedure and conclusions are presented here. A preliminary step was to construct graphs of vertical and horizontal isotachs of the flow field around the oblate spheroid. Fig. 7 depicts such fields, normalized with respect to $V_{L\infty}$, about an oblate spheroid of ice having a semi-major axis of 404 μm and an axis ratio 0.05. Sphere trajectories relative to the oblate spheroid were superimposed on these graphs, from which the local vertical and horizontal accelerations were found. Since a sphere tended to fall at its terminal velocity with respect to the fluid immediately surrounding it, the sphere's acceleration was proportional to the difference between

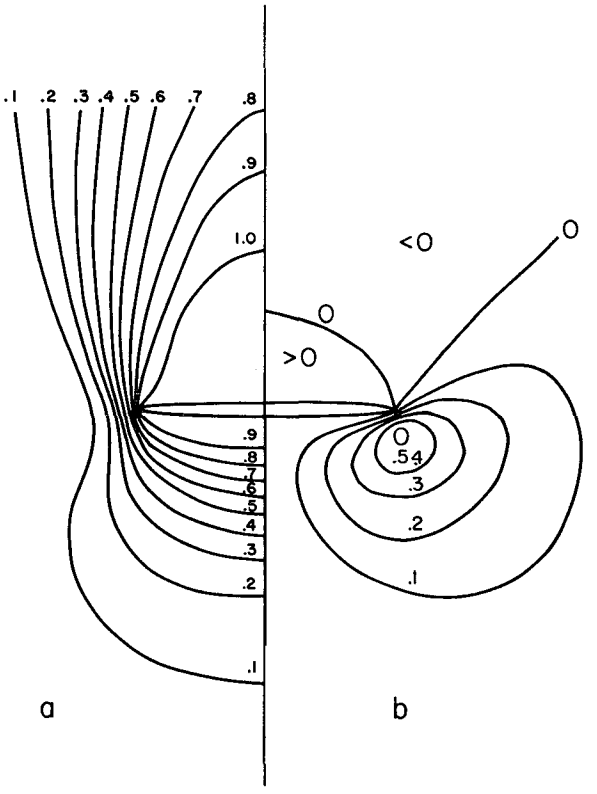

FIG. 7. Normalized isotachs of the flow field around an oblate spheroid for $a_L=404$ μm: (a) vertical isotachs, (b) horizontal isotachs.

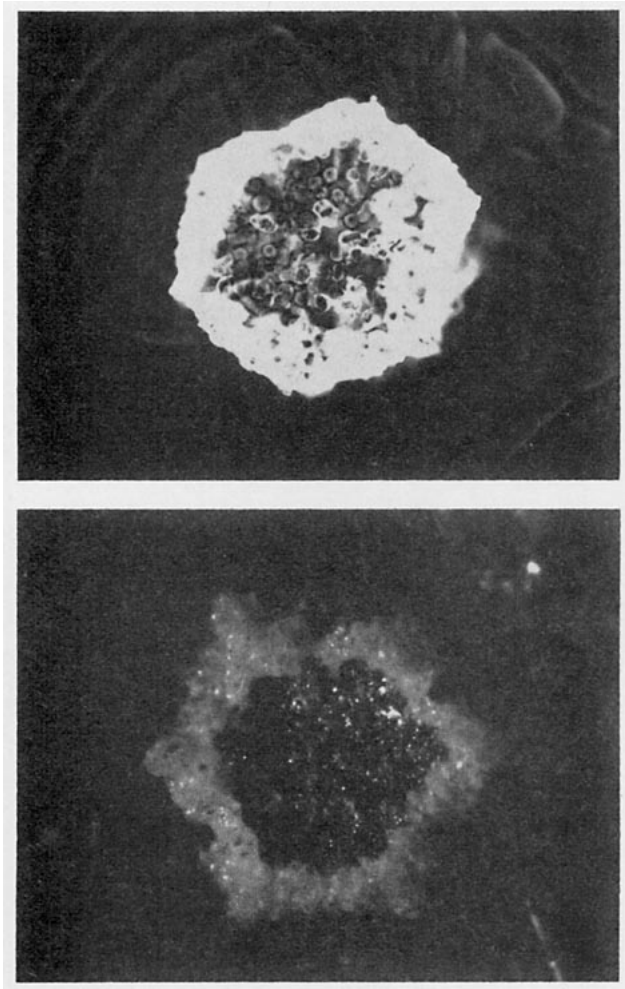

FIG. 8. Rimed hexagonal ice plate showing preferential riming at the edges. (Courtesy of G. Vali.)

the velocity the sphere tended to reach and its actual velocity. If at $y<y_c$, the water sphere was able to accelerate to the terminal velocity of the oblate spheroid of ice before they collided, the horizontal forces successfully moved the sphere around the oblate spheroid and no collision occurred. In order to ascertain that the intersecting trajectories depicted in Figs. 5b and 6b are reasonable, the drop relaxation times were compared to the time of interaction between the sphere and the oblate spheroid. Since the relaxation time was of the order of, or larger than, the interaction time, the results are considered reasonable in this regard. The results presented in Figs. 3–6 follow logically from the results of this analysis. Applied to the atmosphere, the present results predict that a thin hexagonal plate of ice, which has grown to a size at which it can begin colliding with the existing cloud drops, has an annular collision domain and thus collects drops predominantly at its rim. This is in excellent agreement with the field observations of Wilkins and Auer (1970), Zikmunda and Vali (1972) and Knight and Knight (1973), who have presented clear evidence that large numbers of lightly rimed ice crystal plates have much greater concentrations of frozen drops collected on their outer portions (Fig. 8). As Knight and Knight have suggested, such is probably the initial mechanism in the formation of conical graupel.

Acknowledgments. The authors are indebted to the National Science Foundation under Grant NSF GA 32814X. Special thanks go to Drs. G. Vali and A. H. Auer who put at our disposal several excellent pictures of ice crystals collected in atmospheric clouds.

APPENDIX

Derivation of Ice Crystal Equations of Motion

For Reynolds numbers <100, a circular disk or thin oblate spheroid falls stably with its broadest extension perpendicular to the flow so that its axis of symmetry is parallel to the axis of the flow. Thus, the trajectories of a large oblate spheroidal ice crystal and a small spherical water drop are governed by the equations of motion

$$m_L\frac{d\mathbf{V}_L}{dt}=m_L\mathbf{g}-\frac{\pi}{4}\mu c_{DL}N_{\mathrm{Re}L}a_L(\mathbf{V}_L-\mathbf{U}_S), \tag{1}$$

$$m_S\frac{d\mathbf{V}_S}{dt}=m_S\mathbf{g}-\frac{\pi}{4}\mu c_{DS}N_{\mathrm{Re}S}a_S(\mathbf{V}_S-\mathbf{U}_L), \tag{2}$$

where the symbols presented in the equations appearing in the appendix are defined in the List of Symbols at the end of this Appendix. The buoyancy terms $(\rho_L-\rho)/\rho_L$ and $(\rho_S-\rho)/\rho_S$ have been omitted from the gravitational terms of the above equations. The simplification results in an error of about 0.1%. These equations are nondimensionalized by the relations

$$\left.\begin{aligned}&\mathbf{V}^*=\mathbf{V}/V_{L\infty}, \qquad \mathbf{U}^*=\mathbf{U}/V_{L\infty}\\ &\mathbf{g}^*=\mathbf{g}a_L/V_{L\infty}^2, \qquad t^*=tV_{L\infty}/a_L\\ &\mu^*=\mu a_L^2/(m_LV_{L\infty}),\end{aligned}\right\} \tag{3}$$

where $V_{L\infty}=|\mathbf{V}_{L\infty}|$, $\mathbf{V}$ and $\mathbf{U}$ are the velocities of the falling object and of the air due to the motion of the object, m the mass of the object, and μ the dynamic viscosity of the air. Subscripts L and S denote the large oblate spheroid and the small sphere, respectively. During the interaction of the ice crystal and water drop the drag coefficients c_{DL} and c_{DS} vary due to accelerations and non-uniform flow about the bodies. These variations in c_D were not taken into account in our computations. In each case c_D was taken as that for a body at terminal velocity in an undisturbed medium. An *a posteriori* analysis of the accelerations and the flow non-uniformity involved in the cases studied showed that this simplification was justified. The effects of accelerations and flow non-uniformity on c_{DS} and c_{DL} were found to be insufficient to noticeably affect the computed trajectories and collision efficiencies.

Utilizing the relations in Eq. (3), Eq. (1) is written in nondimensional form as

$$\frac{d\mathbf{V}_L^*}{dt^*}=\mathbf{g}^*-\frac{\pi}{4}\mu^* c_{DL} N_{\mathrm{Re}L}(\mathbf{V}_L^*-\mathbf{U}_S^*). \tag{4}$$

In the case of the oblate spheroid falling at terminal velocity in an undisturbed, unbounded fluid (since $U_S^*=0$ $V_L^*=V_{L\infty}^*=1$ and $dV_L^*/dt^*=0$), the vertical component of Eq. (4) is

$$|\mathbf{g}^*|=\frac{\pi}{4}\mu^* c_{DL} N_{\mathrm{Re}L}. \tag{5}$$

The scalar magnitude of the nondimensional acceleration of gravity (designated Q_1) is written

$$Q_1=\frac{\pi}{4}\mu^* c_{DL} N_{\mathrm{Re}L}, \tag{6}$$

where Q_1 is dependent on variables which are constant for a given ice crystal and environment. The ratios p and q are defined by

$$\left.\begin{aligned} p&=a_S/a_L\\ q&=\rho_L/\rho_S \end{aligned}\right\}.$$

Since

$$m_L=4\pi a_L^2 b\rho_L/3=4\pi a_L^3 AR\rho_L/3,$$

and

$$m_S=4\pi a_S^3\rho_S/3,$$

then

$$\left.\frac{m_L}{m_S}=\frac{a_L^3\rho_L AR}{a_S^3\rho_S}=\frac{qAR}{p^3}\right\}. \tag{7}$$

Eq. (2) is written in nondimensional form as

$$\frac{d\mathbf{V}_S^*}{dt}=\mathbf{g}^*-\frac{\pi}{4}c_{DS}N_{\mathrm{Re}S}p\frac{m_L}{m_S}\mu^*(\mathbf{V}_S^*-\mathbf{U}_L^*). \tag{8}$$

Eq. (7) is utilized to obtain

$$\frac{d\mathbf{V}_S^*}{dt}=\mathbf{g}^*-\frac{\pi c_{DS}N_{\mathrm{Re}S}qAR\mu^*}{4p^2}(\mathbf{V}_S^*-\mathbf{U}_L^*). \tag{9}$$

For convenience, the parameter Q_2 is designated

$$Q_2=\frac{\pi c_{DS}N_{\mathrm{Re}S}qAR\mu^*}{4p^2}, \tag{10}$$

where Q_2 is dependent on variables which are constant for a given ice crystal, water drop and environment.

In order to obtain the trajectories of ice crystals and water drops, it is necessary to know the parameters $\mathbf{U}$ and c_D for each body. These results for the sphere were determined by the numerical results of LeClair *et al.* (1970). The results for the oblate spheroid were those for axis ratio 0.05 which were obtained by Pitter *et al.* (1973).

TABLE 1. Size and terminal velocity of oblate spheroids of density 0.92 gm cm^{-3} in atmosphere of -10C, 700 mb ($\rho=9.267\times10^{-4}$ gm cm^{-3}, $\mu=1.667\times10^{-4}$ poise).

$N_{\mathrm{Re}L}$	c_{DL}	a_L (μm)	V (cm sec^{-1})
0.1	207.14	50.6	1.78
0.5	43.54	87.9	5.12
1.0	23.02	113.0	7.97
2.0	12.67	147.0	12.25
2.5	10.53	160.0	14.04
4.0	7.28	194.0	18.57
5.0	6.17	213.0	21.14
10.0	3.87	289.0	31.11
20.0	2.63	404.0	44.59

It is also necessary to know the size and terminal velocity of an oblate spheroid of given Reynolds number and drag coefficient. Considering the vertical component of Eq. (1) for the case of an oblate spheroid falling at terminal velocity in an infinite, undisturbed environment, and including the buoyancy mentioned previously, one obtains

$$c_{DL}N_{\mathrm{Re}L}=\frac{4m_L g(\rho_L-\rho)}{\pi\mu a_L V_{L\infty}\rho_L}. \tag{11}$$

Multiplying Eq. (11) by $N_{\mathrm{Re}_L}=2a_L V_{L\infty}\rho/\mu$ and expressing $m_L=4\pi a_L^3 AR\rho_L/3$, one obtains

$$c_{D_L}N_{\mathrm{Re}_L}^2=32ga_L^3AR(\rho_L-\rho)\rho/(3\mu^2). \tag{12}$$

Solving for a_L, we have

$$a_L=[3\mu^2 c_{D_L}N_{\mathrm{Re}_L}^2/32gAR(\rho_L-\rho)\rho]^{\frac{1}{3}}. \tag{13}$$

It is assumed that $\rho_L=\rho_{\mathrm{ice}}=0.92$ gm cm^{-3}, $\rho_S=\rho_{\mathrm{water}}=1$ gm cm^{-3}, and $\rho=\rho_{\mathrm{air}}=9.267\times10^{-4}$ gm cm^{-3} in the present studies. The terminal velocity of the oblate spheroid of ice is found by

$$V_{L\infty}=\mu N_{\mathrm{Re}}/(2a_L\rho). \tag{14}$$

Values for a_L and $V_{L\infty}$ for the oblate spheroid are given in Table 1.

Since velocity is the time derivative of position, the relation

$$\frac{d\mathbf{R}}{dt}=\mathbf{V} \tag{15}$$

applies for the time variation of the position of either the oblate spheroid or the sphere. A system of eight first-order ordinary differential equations can be specified for the sphere and oblate spheroid trajectories by resolving Eqs. (15), (4) and (9) into their cylindrical (z,y) components and utilizing Eqs. (6) and (10) for convenience. [Eqs. (16) and (17) are nondimensional;

asterisks are dropped for clarity.]

$$\left.\begin{aligned}
&\frac{dR_{Lz}}{dt}=V_{Lz}\\
&\frac{dV_{Lz}}{dt}=Q_1[1-(V_{Lz}-U_{Sz})]\\
&\frac{dR_{Ly}}{dt}=V_{Ly}\\
&\frac{dV_{Ly}}{dt}=-Q_1(V_{Ly}-U_{Sy})\\
&\frac{dR_{Sz}}{dt}=V_{Sz}\\
&\frac{dV_{Sz}}{dt}=Q_1-Q_2(V_{Sz}-U_{Lz})\\
&\frac{dR_{Sy}}{dt}=V_{Sy}\\
&\frac{dV_{Sy}}{dt}=-Q_2(V_{Sy}-U_{Ly})
\end{aligned}\right\}. \tag{16}$$

The first four equations of Eq. (16) govern the vertical and horizontal time derivatives of position and velocity of the ice crystal. The last four equations govern those of the water drop. The **U**-field due to the motion of the ice crystal was evaluated from the results of Pitter *et al.*, at grid points in oblate spheroidal coordinates with the radial step size $\Delta\xi=0.1$ and angular step size $\Delta\eta=6°$. The **U**-field due to the motion of the water drop was evaluated from the results of LeClair *et al.*, at grid points in modified spherical coordinates with radial step size $A=0.05$ and angular step size $B=3°$. Beyond the outer boundaries used to determine the flow fields, the fluid was assumed to be unperturbed by the presence of the moving body. Outer boundaries were located at 64 crystal semi-major axis lengths and 90 drop radii.

These equations were solved numerically using Hamming's predictor-corrector-modifier method, with a Runge-Kutta method used to start the integration. The integration routine is found in IBM manual H20-02053 (Anonymous, 1968). The subroutine was directly accessible on the IBM 360/91 computer used in the present study. Both the Hamming and Runge-Kutta schemes are of fourth-order accuracy, and both contain error controls. During the integration of the trajectories, it was assumed that each body experienced external forces due to the presence of the other body as though the **U**-field due to the second body acted at the center of the first body. **U**-fields were evaluated at specific points using double linear interpolation in the appropriate coordinate systems.

Vertical and horizontal separation between the centers of the oblate spheroid and the sphere are determined by

$$\left.\begin{aligned}
\Delta z&=R_{Sz}-R_{Lz}\\
\Delta y&=R_{Sy}-R_{Ly}
\end{aligned}\right\}. \tag{17}$$

Using the method just outlined, trajectories were computed for the interacting thin oblate spheroidal ice crystals and spherical water drops in order to determine the critical grazing trajectory, at which the water drop just touches the ice crystal during the interaction. From these results, the collision efficiency E was determined by the relation

$$E=\frac{\pi r_c^2}{\pi(a_L+a_S)^2}, \tag{18}$$

where r_c is the initial horizontal offset of the sphere center from the axis of symmetry of the flow field around the crystal. In nondimensional form, Eq. (18) becomes

$$E=\frac{\pi y_c^2}{\pi(1+p)^2}=\frac{y_c^2}{(1+p)^2}. \tag{19}$$

Since the present results reveal that a collision-free region may exist for some $y<y_{\min}\leqslant y_c$, it is necessary to express the collision efficiency using a more complete relation than Eq. (19). Thus, the expression

$$E=\frac{y_c^2-y_{\min}^2}{(1+p)^2} \tag{20}$$

correctly defines E when drops with $y_{\min}\leqslant y\leqslant y_c$ collide with the oblate spheroidal ice crystal.

List of Symbols

a	radius of body normal to flow
AR	axis ratio
c_D	drag coefficient
E	collision efficiency
g, $\mathbf{g}$	acceleration of gravity
L	subscript denoting large body (oblate spheroid)
m	mass
N_{Re}	Reynolds number
p	size ratio $[=a_S/a_L]$
Q_1, Q_2	nondimensional drag parameters
q	density ratio $[=\rho_L/\rho_S]$
$\mathbf{R}$	position vector
r_c	initial horizontal offset of critical grazing trajectory
S	subscript denoting small body (sphere)
t	time

$\mathbf{U}$	velocity of fluid due to motion of body
$\mathbf{V}$	velocity of body
V_∞	terminal velocity
y	subscript denoting horizontal component; initial nondimensional horizontal offset
y_c, $y_{\min}$	initial critical nondimensional horizontal offsets
z	subscript denoting vertical component
Δy, Δz	horizontal and vertical separation of centers
μ	dynamic viscosity
ρ	density.

REFERENCES

Anonymous, 1968: System/360 scientific subroutine package. No. H20-0205-3, IBM, New York, 454 pp.

Beard, K. V., and H. R. Pruppacher, 1971: A wind tunnel investigation of collection kernels for small water drops in air. *Quart. J. Roy. Meteor. Soc.*, **97**, 242–248.

Braham, R. R., 1968: Meteorological bases for precipitation development. *Bull. Amer. Meteor. Soc.*, **49**, 343–353.

Danielson, E. F., R. Bleck and D. A. Morris, 1972: Hail growth by stochastic collection in a cumulus model. *J. Atmos. Sci.*, **29**, 135–155.

Davies, C. M., and C. V. Peetz, 1956: Impingement of particles on a transverse cylinder. *Proc. Roy. Soc. London*, **A234**, 269–295.

Jayaweera, K. O. L. F., and R. E. Cottis, 1969: Fall velocities of plate-like and columnar crystals. *Quart. J. Roy. Meteor. Soc.*, **95**, 703–709.

Kajikawa, M., 1972: Measurement of falling velocities of individual snow crystals. *J. Meteor. Soc. Japan*, Ser. 2, **50**, 577–583.

Klett, J. D., 1968: The interaction and motion of rigid spheres falling in a viscous fluid at low Reynolds numbers. Ph.D. dissertation, University of California, Los Angeles, 113 pp.

——, and M. H. Davis, 1973: Theoretical collision efficiencies of cloud droplets at small Reynolds numbers. *J. Atmos. Sci.*, **30**, 107–117.

Knight, C. A., and N. C. Knight, 1973: Conical graupel. *J. Atmos. Sci.*, **30**, 118–124.

Langmuir, I., 1948; The production of rain by a chain-reaction in cumulus clouds at temperatures above freezing. *J. Meteor.*, **5**, 175–192.

LeClair, B. P., A. E. Hamielec and H. R. Pruppacher, 1970: A numerical study of the drag on a sphere at low and intermediate Reynolds numbers. *J. Atmos. Sci.*, **27**, 308–315.

List, R., and R. S. Schemenauer, 1971: Free fall behavior of planar snow crystals, conical graupel and small hail. *J. Atmos. Sci.*, **28**, 110–115.

Mason, B. J., 1971: *The Physics of Clouds*, 2nd ed. Oxford, Clarendon Press, 671 pp.

Musil, D. J., 1970: Computer modeling of hailstone growth in feeder clouds. *J. Atmos. Sci.*, **27**, 474–482.

Ono, A., 1969: The shape and riming properties of ice crystals in natural clouds. *J. Atmos., Sci.*, **26**, 138–147.

Picknet, R. G., 1960; Collection efficiencies for water drops. *Intern. J. Air Pollution*, **3**, 160–168.

Pitter, R. L., H. R. Pruppacher and A. E. Hamielec, 1973: A numerical study of the viscous flow past a thin oblate spheroid at low and intermediate Reynolds numbers. *J. Atmos. Sci.*, **30**, 125–134.

Ranz, W. E., and Wong, J. B., 1952: Impaction of dust and smoke particles. *Ind. Eng. Chem.*, **44**, 1371–1380.

Shafrir, U., and T. Gal-Chen, 1971: A numerical study of collision efficiencies and coalescence parameters for droplet pairs with radii up to 300 microns. *J. Atmos. Sci.*, **28**, 741–751.

——, and M. Neiburger, 1963: Collision efficiencies of two spheres falling in a viscous medium. *J. Geophys. Res.*, **69**, 4141–4147.

Steinberger, E. H., H. R. Pruppacher and M. Neiburger, 1968: On the hydrodynamics of pairs of spheres falling along their line of centers in a viscous medium. *J. Fluid Mech.*, **34**, 808–819.

Takeda, T., 1968a: Solid precipitation in a supercooled cloud. Part 1. *J. Meteor. Soc. Japan*, **46**, 14–28.

——, 1968b: Solid precipitation in a supercooled cloud. Part 2. *J. Meteor. Soc. Japan*, **46**, 255–265.

Wilkins, R. I., and A. H. Auer, 1970; Rimming properties of hexagonal ice crystals. *Preprints Conf. Cloud Physics*, Fort Collins, Colo.. Amer. Meteor. Soc., 81–82.

Woods, J. D., and B. J. Mason, 1964: Experimental determination of collection efficiencies for small water drops in air. *Quart. J. Roy. Meteor. Soc.*, **93**, 373–381.

——, and ——, 1965; The wake capture of drops in air. *Quart. J. Roy. Meteor. Soc.*, **91**, 35–43.

Zikmunda, J., and G. Vali, 1972: Fall patterns and fall velocities of rimed ice crystals. *J. Atmos. Sci.*, **29**, 1334–1347.